

Postembedding Iodine Staining for Contrast-Enhanced 3D Imaging of Bone Tissue Using Focused Ion Beam-Scanning Electron Microscopy

Mahdi Ayoubi, Richard Weinkamer, Alexander F. van Tol, Maximilian Rummmler, Paul Roschger, Peter C. Brugger, Andrea Berzlanovich, Luca Bertinetti,* Andreas Roschger,* and Peter Fratzl*

For a better understanding of living tissues and materials, it is essential to study the intricate spatial relationship between cells and their surrounding tissue on the nanoscale, with a need for 3D, high-resolution imaging techniques. In the case of bone, focused ion beam-scanning electron microscopy (FIB-SEM) operated in the backscattered electron (BSE) mode proves to be a suitable method to image mineralized areas with a nominal resolution of 5 nm. However, as clinically relevant samples are often resin-embedded, the lack of atomic number (Z) contrast makes it difficult to distinguish the embedding material from unmineralized parts of the tissue, such as osteoid, in BSE images. Staining embedded samples with iodine vapor has been shown to be effective in revealing osteoid microstructure by 2D BSE imaging. Based on this idea, an iodine ($Z = 53$) staining protocol is developed for 3D imaging with FIB-SEM, investigating how the amount of iodine and exposure time influences the imaging outcome. Bone samples stained with this protocol also remain compatible with confocal laser scanning microscopy to visualize the lacunocanalicular network. The proposed protocol can be applied for 3D imaging of tissues exhibiting mineralized and nonmineralized regions to study physiological and pathological biomineralization.


1. Introduction

Considerable progress has been made in the 3D imaging of mineralized tissues with X-rays or electrons.^[1–5] The simultaneous imaging of organic and mineral components remains challenging because of the comparatively low electron density of the organic component.^[6] This challenge is particularly evident in resin-embedded samples, where the necessary imaging contrast between different soft tissues, or between soft tissue and embedding material, often requires staining methods.^[7] Bone is a paradigmatic example of such a challenging material,^[8] for which determining pathology and treatments relies heavily on its structural characterization. Histological preparation of undecalcified samples typically involves embedding samples in resin.^[6,7,9–11] Imaging such clinically relevant specimens with focused ion beam-scanning electron microscopy (FIB-SEM) in 3D, therefore,

necessitates an optimized staining protocol. As the close proximity of the bone cells to the extracellular matrix involves osteocytes and

M. Ayoubi,^[†] R. Weinkamer, A. F. van Tol, M. Rummmler, P. Fratzl
Department of Biomaterials
Max Planck Institute of Colloids and Interfaces
14476 Potsdam, Germany
E-mail: fratzl@mpikg.mpg.de

M. Ayoubi, A. F. van Tol
Berlin-Brandenburg School of Regenerative Therapies (BSRT)
Charité Campus Virchow-Klinikum
D-13353 Berlin, Germany

 The ORCID identification number(s) for the author(s) of this article can be found under <https://doi.org/10.1002/anbr.202400035>.

^[†]Present address: Department of Materials Science and Engineering, Cornell University, Ithaca, NY 14853, USA

© 2024 The Author(s). Advanced NanoBiomed Research published by Wiley-VCH GmbH. This is an open access article under the terms of the Creative Commons Attribution License, which permits use, distribution and reproduction in any medium, provided the original work is properly cited.

DOI: 10.1002/anbr.202400035

P. Roschger
Ludwig Boltzmann Institute of Osteology
Hanusch Hospital of OEGK and AUVA Trauma Centre
A-1140 Vienna, Austria

P. C. Brugger
Department of Anatomy
Center for Anatomy and Cell Biology
Medical University of Vienna
A-1090 Vienna, Austria

A. Berzlanovich
Center of Forensic Science
Medical University of Vienna
Sensengasse 2, A-1090 Vienna, Austria

L. Bertinetti
B CUBE—Center for Molecular Bioengineering
Technische Universität Dresden
01307 Dresden, Germany
E-mail: luca.bertinetti@tu-dresden.de

its associated lacunocanicular network (LCN),^[12] a correlative imaging approach to characterizing the LCN and the 3D tissue structure yields the most complete view of the mineralized and nonmineralized components of the LCN.

A common approach to preserving bone tissues is to embed them in a resin, such as polymethylmethacrylate (PMMA),^[13] paraffin,^[14] or epoxy,^[15,16] which has the crucial advantages of avoiding shrinkage^[17] and distortion of the tissue,^[18] facilitating surface grinding and polishing,^[19] and allowing for long-term archiving. PMMA is frequently used when an optimal penetration of the resin into bone is required.^[7] Methacrylates are also advantageous over other embedding resins because they are less likely to cause tissue shrinkage^[13] and because they help avoid demineralization.^[20]

Embedding has the additional benefit of providing material integrity for imaging techniques for which a smooth sample is needed and those that are sectioned with a knife, such as histology and serial block-face scanning electron microscopy.^[4] However, the backscattered electron (BSE) coefficient η for the organic matrix is low ($\eta \approx 0.07$), thus making it difficult to distinguish between osteoid and PMMA in resin-embedded bone samples.^[21,22] As a consequence, the PMMA-filled porous substructures in bone, like the aforementioned LCN or the larger Haversian canals, cannot be distinguished from the osteoid.

Many en bloc staining protocols based on heavy elements are known for Z contrast enhancement, which must be used before embedding. Uranyl acetate,^[23] osmium tetroxide,^[24] phosphotungstic acid,^[25] and Lugol solution containing iodine^[18] have been widely used for the staining of the organic matrix, such as for collagen in rat incisors and tail tendons,^[26] turkey leg tendons,^[27] porcine iliac vein vascular tissues,^[28] and mouse muscle fibers.^[29] Iodine in its vapor phase has also been used for staining soft tissue including chondrocytes in a mouse tibia's growth plate,^[30] and a locust head's chitin exoskeleton, muscle, and nerves.^[31]

Imaging resin-embedded bone specimens necessitates reliable methods for staining the bone tissues. Boyde et al. have proposed two postembedding protocols based on iodine: 1) a liquid staining protocol using Lugol solution,^[32] and 2) a vapor staining protocol using gaseous iodine (I_2).^[31] The liquid staining protocol (1) enables staining close to the sample surface for bone, cartilage, and muscle tissues in different animals including mice, rats, horses, and elephants, as well as implant sites such as the human jaw, rabbit tibia, and dog maxilla, thus allowing 2D BSE imaging. The vapor protocol (2) similarly enables staining the bone tissues of different samples including human, horse, rat, and mouse for 2D BSE imaging, in turn allowing investigation of the soft-hard tissue interfaces, such as an interface between calcified and uncalcified cartilage.^[31] Although the liquid staining protocol (1) is rapid (2–15 min) in comparison with the vapor staining protocol ((2), days to weeks), the latter is beneficial for avoiding problems associated with the liquid medium, such as limited iodine penetration (due to iodine's solvent characteristics), the accumulation of iodine on the surface, and pooling of the stain around cracks

and defects.^[31] Gaseous iodine diffuses through PMMA, and stains the tissue mainly via reacting with unsaturated molecules' carbon-carbon double bonds.^[31]

To further expand the capabilities of postembedding staining, in this article, an iodine vapor staining protocol aimed at further expanding the capabilities of postembedding staining for 3D BSE FIB-SEM imaging of bone tissue is presented. This protocol was recently successfully employed in an investigation of substructures in the mineralization front to elucidate the role of the LCN in early mineralization stages.^[33] In the current work, the effect of changing staining time, the amount of stain, and laser irradiation on image quality is reported and potential advantages and disadvantages when modifying these parameters are discussed. Similar to Boyde et al.'s protocol, the approach presented allows for a discrimination between the main three compartments of a PMMA-embedded bone sample, i.e., mineralized bone, osteoid, and embedding material, not only in 2D but in 3D (see the caption of **Figure 1** as well as Figure 6 for more details). Importantly, this protocol offers the possibility to reinvestigate numerous unique clinically relevant bone samples which were embedded and archived years or decades ago.

The goal of the present work was to develop a staining protocol that allows the 3D characterization of both, the LCN in bone, as well as the nanoscale structure of its mineralized and unmineralized tissue components in the same specimen. We describe the optimal procedure and report the effects of varying staining parameters on the imaging outcome.

2. Results

The results of 16 3D image stacks across seven samples are presented here to show the characteristics of different staining protocols. With the exception of samples #1 and #2, all samples were stained differently. Six different experimental protocols were explored (**Table 1**) and the results are accordingly presented in three sections: First, protocol #1, which is a recommendation for FIB-SEM studies on bone samples including both osteoid and mineralized bone. Second, the results of investigating any possible interference between the two used imaging techniques, i.e., confocal laser scanning microscopy (CLSM) and FIB-SEM, to determine the possibility of combining them for a thorough characterization of the LCN in the bone (protocols #2, #3, and #4). Finally, the influence of the main parameters of iodine staining—incubation time and amount of iodine—on the FIB-SEM image quality (protocols #5 and #6). Additionally, the surface effect of iodine staining was investigated. The main compartments of the bone samples imaged and analyzed in this study are mineralized bone, osteoid (newly formed, still unmineralized bone), soft tissue (osteoid, cells, membranes, blood vessels, etc.), and porosity (all spaces accessible and consequently filled with PMMA during embedding, including Haversian canals, osteocyte lacunae, and canaliculi).

2.1. Staining Bone Tissue for Combined Imaging with FIB-SEM and CLSM

Two human femoral midshaft samples were stained with rhodamine followed by embedding and postembedding iodine vapor

A. Roschger
Department for Chemistry and Physics of Materials
Paris Lodron University of Salzburg
5020 Salzburg, Austria
E-mail: andreas.roschger@plus.ac.at

staining according to protocol #1 (see Table 1). Subsequently, six 3D FIB-SEM and CLSM image stacks were obtained, resulting in image stacks suitable for segmentation of 1) the mineralized bone, 2) the osteoid, and 3) the LCN. Hence, in addition to the staining protocol, a routine for segmentation of these three

compartments is also described. Figure 1a,b shows environmental scanning electron microscopy (ESEM) images of a forming osteon before and after iodine staining from the sample surface. The most salient features of these images are the central, almost black, Haversian canal and the dark gray value of the whole

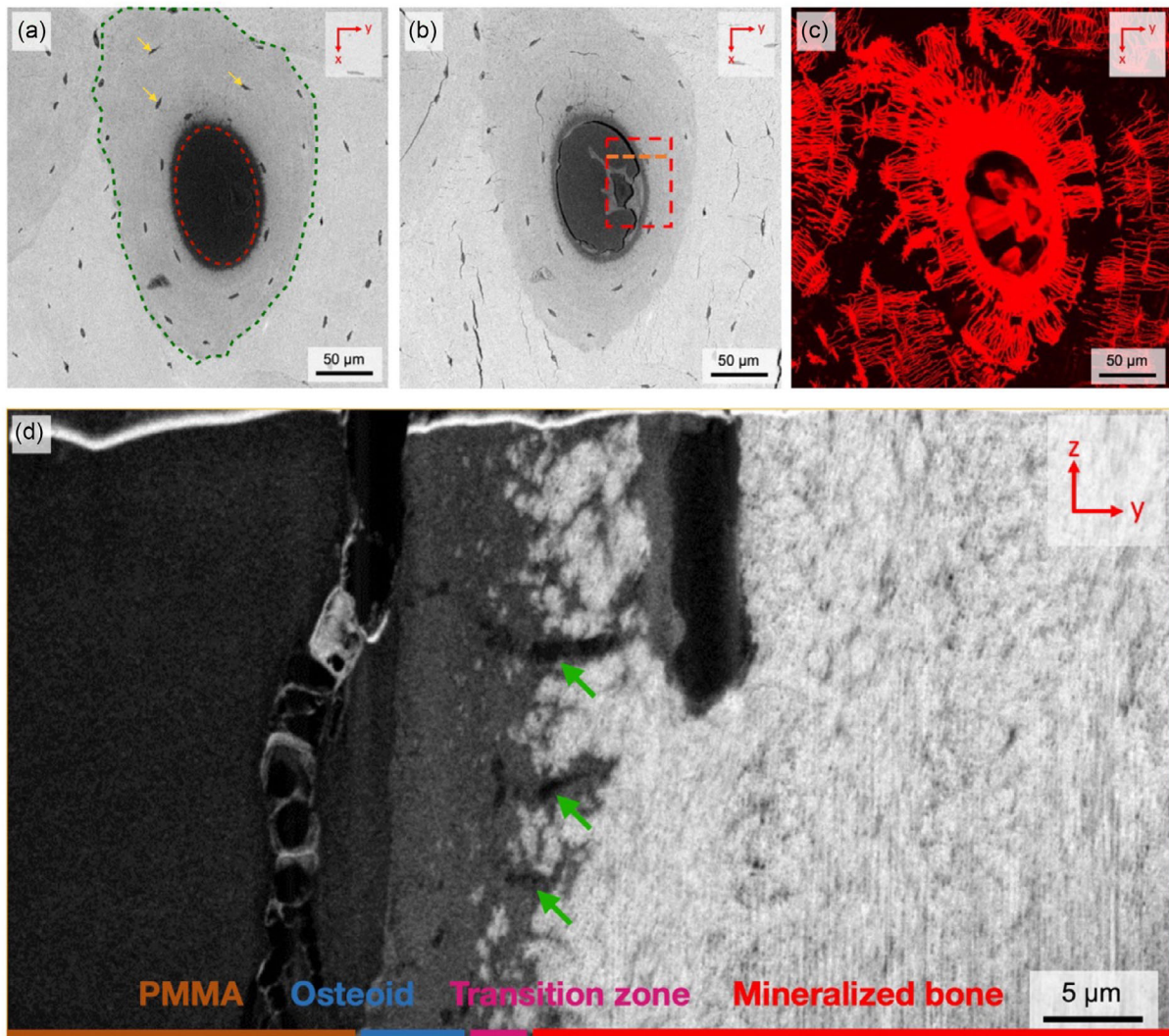


Figure 1. Imaging of a forming osteon (osteon #1 of sample #1). An osteon, or Haversian system (surrounded by a dashed green line in a), is the building block of the cortical bone and is composed of a Haversian canal (the dashed red oval in (a)) where blood vessels and nerves exist.^[74] The Haversian canal is surrounded by concentric lamellae made of mineralized collagen fibers. During bone formation, osteocytes differentiate from osteoblasts and reside in lacunae (the yellow arrows in (a)) and canaliculi, which contain dendritic osteocyte processes. The lacunae and canaliculi together form a dense LCN within an osteon c). Three different imaging techniques (ESEM, CLSM, and FIB-SEM) were used to image the osteon and its compartments. Panels (a) and (b) are BSE images obtained by ESEM before and after iodine staining, respectively, using protocol #1. The dashed red rectangle in (b) shows the region of interest milled by a FIB. The orange dashed line within the region of interest shows the location of the slice of the FIB-SEM image stack shown in panel d). Panel (c) shows the LCN with CLSM after rhodamine staining and the result of the maximum intensity projection of the first 30 consecutive slices of the CLSM stack (wherein the pixel brightness corresponds to the maximum intensity within the z-stack for given x–y coordinates). Panel (d) is a FIB-SEM BSE image showing a 2D slice of a 3D image stack. The green arrows indicate the cross section of the canaliculi and the orthoslice. Panel e) shows the gray value frequency distribution of the corresponding 3D FIB-SEM image stack. The three peaks in the graph refer to the distinction of three different regions in the forming osteon: the mineralized bone (whitish), the stained osteoid (dark gray), and PMMA (black); m denotes the minimum between the peaks corresponding to mineralized bone and osteoid, Δm is defined as 5% of the distance between the peaks, d . Panel f) is the result obtained after image segmentation: 3D rendering of the osteocyte LCN (green) and the Haversian canal (brown) to the left of the panel. The orthoslices show perpendicular BSE images of the FIB-SEM image stack. In (a–d), the orientation of the images can be deduced by the 2D coordinate system in the upper right corner of the images in relation to the 3D coordinate system of the schematic osteon in panel (f) (z-axis aligned with the longitudinal axis of the osteon).

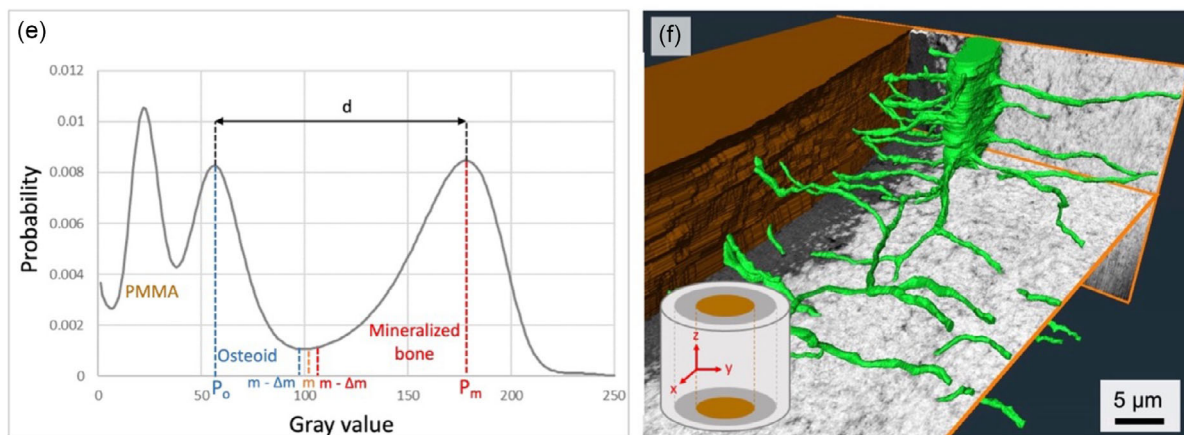


Figure 1. Continued.

Table 1. Overview of the six different experimental protocols for 3D imaging of bone tissue using CLSM and FIB-SEM. Protocol #1 (standard protocol) refers to the protocol recommended for optimal contrast between mineralized bone, osteoid, and PMMA. In the FIB-SEM BSE images, red, blue, and brown bars correspond to the mineralized bone, osteoid, and PMMA, respectively. The field of view of the images is $\approx 40 \mu\text{m}$.

Protocols	#1	#2	#3	#4	#5	#6
Main feature	Standard protocol	No CLSM	No rhodamine No CLSM	CLSM before iodine staining	Long incubation	Extra iodine
Rhodamine staining	Yes	Yes	No ^{a)}	Yes	Yes	Yes
Iodine staining [mg]	$2 \times 0.1^{\text{a)}$	2×0.1	2×0.1	2×0.1	4×2	$50^{\text{a)}$
Incubation time [days]	$2 \times 6^{\text{a)}$	2×6	2×6	2×6	$35^{\text{a)}$	7
Time lag between staining cycles	11 days (sample #1) 4 days (sample #2)	11 days	No time lag	24 days	No time lag	–
CLSM	Yes (after iodine staining) ^{a)}	No ^{a)}	No ^{a)}	Yes (before iodine staining) ^{a)}	No	No
Sample no.	Sample #1 and #2	Sample #3	Mouse femur	Sample #4	Sample #5	Sample #6
Number of datasets	6 datasets	3 datasets	2 datasets	3 datasets	1 dataset	1 dataset
FIB-SEM BSE images						

^{a)}The critical parameter(s) distinguishing each protocol.

osteone, which set them apart from the surrounding, brighter, interstitial bone. The major differences between the two images are the brighter osteoid around the Haversian canal after staining and the soft tissue fragments inside the canal as shown in Figure 1b. This distinction between the Haversian canal and the osteoid after iodine staining becomes even clearer in the higher resolution FIB-SEM BSE image (Figure 1d), which reveals more structural details: to the left is the Haversian canal filled with PMMA, then the osteoid (dark gray), with the mineralized bone as the bright phase further to the right. The transition between the osteoid and mineralized bone has a cloudy appearance with isolated mineralization foci within the osteoid. At the top of the image is an osteocyte lacuna close to the transition zone between the osteoid and mineralized bone. The lacuna is

filled with PMMA and, therefore, appears black and is surrounded by soft tissue (dark gray). Other elongated black structures correspond to PMMA-filled canaliculi emanating from the lacuna (green arrows).

The gray value frequency distribution (normalized and, therefore, expressed as a probability) of 8-bits BSE images acquired during FIB-SEM imaging shows three clearly separated peaks, which demonstrate a distinction between PMMA-filled porosity, osteoid, and mineralized bone (Figure 1e). By using Amira (Version 2019.38, Zuse Institute Berlin (ZIB), Berlin, Germany), PMMA-filled porosity was first segmented following the method used in a previous study,^[33] resulting in a 3D rendering of the lacuna and the surrounding canaliculi (Figure 1f). Second, again following the previous study,^[33] the

distinction between the iodine-stained osteoid and mineralized bone was made by thresholding based on the peak positions of the osteoid (P_o) and the mineralized bone (P_m) and the minimum value (m) between the peaks in the gray value frequency distribution (Figure 1e). See ref. [34] for other thresholding methods.

As the sample was not only stained with iodine, but also with rhodamine, the architecture of the LCN on a larger length scale was imaged by nondestructive CLSM before FIB-SEM was performed (Figure 1c). Thanks to its small size ($<0.5 \text{ nm}^3$, Lu & Penzkofer, 1986), rhodamine penetrates through all accessible porosities, including the LCN, and binds to the surfaces of mineralized bone (such as the walls of the canaliculi) as well as the osteoid, blood vessels, and cells. The images produced by CLSM showed that most of the canaliculi are oriented toward the Haversian canal as reported previously.^[35]

Protocol #1 fulfills the following criteria: 1) iodine staining produces a clear discrimination between osteoid and the embedding material (PMMA) (Figure 1d); 2) the penetration of the iodine staining is spatially homogeneous, therefore allowing 3D imaging of the osteoid and mineralized bone using FIB-SEM; 3) CLSM imaging can precede FIB-SEM, thus providing an image of the large-scale architecture of the LCN using the rhodamine staining of the sample (Figure 1c); and 4) achieving sub-micrometer resolution and sufficiently high signal-to-noise ratio for segmentation in a relatively short time (in this case a structural characterization of bone was produced within roughly 2 weeks from the beginning of the staining).

2.2. Interference Between Iodine Staining, Rhodamine Staining, and CLSM Imaging

A set of experiments were developed to determine whether staining and imaging procedures can be performed independent of each other without compromising effects in image quality due to laser-light-induced chemical reactions.

First, a bone sample (sample #3) was stained with rhodamine and iodine, but no CLSM imaging was performed prior to the FIB-SEM imaging (protocol #2). The ESEM image and BSE image of FIB-SEM after iodine staining (Figure 2a) demonstrate that iodine staining creates the distinctive dark gray zone around the Haversian canal corresponding to unmineralized osteoid. Subsequently, similar FIB-SEM results as those found in protocol #1 were obtained, thus producing segmentation as described above. It was found that the laser irradiation during CLSM measurements does not influence the results of subsequent FIB-SEM imaging. When performing only iodine staining and omitting rhodamine staining and CLSM imaging, it was likewise found that there was no indication of a decrease in iodine staining quality in a sample of murine bone (protocol #3, Figure S1, Supporting Information). These findings seem to suggest that the binding of iodine within the bone tissue is not dominated by a possible substitution of the rhodamine counteranions or by the interaction of (poly)iodides with the cationic dye. Furthermore, iodine staining does not appear to impair CLSM imaging using rhodamine, as image quality remained unchanged when comparing the shown datasets and images obtained in prior studies where no iodine staining was performed.^[36,37]

These findings support the conclusion that the contrast-enhancing effect by iodine staining is both independent from prior staining with rhodamine and from imaging by CLSM performed after the iodine staining. Consequently, if only 3D information on the mineralization of bone is desired using FIB-SEM imaging, all the steps involving rhodamine and CLSM can be skipped, and the sample preparation can be immediately conducted with the iodine staining.

However, protocol #4 demonstrates the caveat that a combination of experimental methods is never a straightforward undertaking. The only difference between this protocol and protocol #1 is that CLSM imaging was performed before iodine staining, and the staining was started less than one hour after CLSM. Figure 2b and S2, Supporting Information, show the imaging results for three different forming osteons with ESEM (Figure 2b(i) and (ii)) and CLSM (Figure 2b(iii)) images on top, a single BSE slice obtained with FIB-SEM in the middle (Figure 2b(iv)), and the corresponding gray value frequency distribution of the whole 3D image stack at the bottom (Figure 2b(v)). Figure 2b(iv) shows that the contrast between the osteoid and mineralized bone became poorer, and this impression is confirmed by the gray value distributions. The “overstaining” with iodine led to a significant reduction of contrast between mineralized bone and osteoid. As a result, the two peaks merged as shown in Figure 2b(v). The laser irradiation of the samples during CLSM imaging seemed to influence the successive iodine staining, resulting in an adverse effect on the contrast of the BSE images.

2.3. Influence of Iodine Amount and Incubation Time of Staining

The two main parameters for the iodine staining protocol are the duration of the sample's exposure to iodine vapor and the intensity of the sample's exposure, determined by the amount of iodine and the volume of the vessel containing the sample and the iodine source. In order to test the effect of longer staining time, an embedded bone sample (sample #5) was placed in the same vessel as the other samples but incubated for 35 days (instead of 12 days as for protocol #1). On average, every 9 days the iodine source was refreshed by placing 2 mg in the vessel, so that over the full time of 35 days 8 mg of iodine were used in total (protocol #5).

Figure 3a shows a FIB-SEM BSE image of one osteon (osteon #1, sample #5) after staining the sample according to protocol #5. As a new feature, the substructure of the osteoid became more apparent when imaged with FIB-SEM, allowing a rough assessment of the orientation of the collagenous matrix (Figure 3a and Movie, Supporting Information). For example, the preferred orientation at the right border of the lacuna seems more in-plane (see the red arrow), while further to the right of the lacuna the orientation changes more to out-of-plane. Although the osteoid still remains darker than the mineralized bone in this protocol, the contrast is distinctly decreased compared to protocol #1, resulting in a substantial overlap of the corresponding peaks in the gray value frequency distribution (Figure 3b). Hence, when segmenting the acquired volume, a simple brightness-based global thresholding—as suggested for protocol #1 (Figure 1)—may not work for protocol #5.

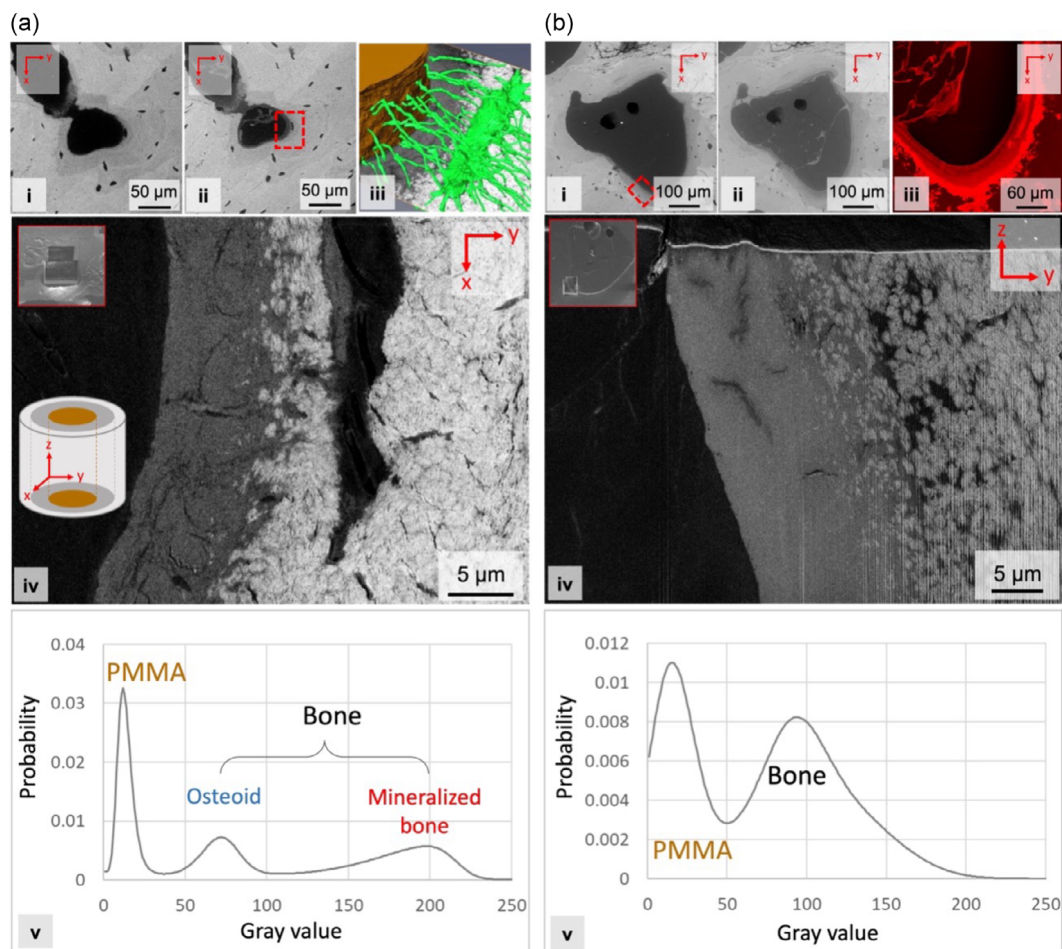


Figure 2. Two different forming osteons with measurement protocols which deviated from protocol #1 in that for a) CLSM was not performed (protocol #2, sample #3, osteon #2) and for b) iodine staining was performed after CLSM imaging (protocol #4, sample #4, osteon #2; two more examples are shown in Figure S2, Supporting Information). Images (i) and (ii) in each panel show the ESEM images before and after iodine staining, respectively. The red dashed rectangle depicts the region of interest for FIB-SEM imaging. Image b(iii) shows the result of the maximum intensity projection of the first 30 consecutive slices of the CLSM stack for the corresponding forming osteon. No CLSM projection is shown for panel (a) because this sample was not imaged with CLSM. Instead, a(iii) shows the 3D rendering of the osteocyte LCN and the Haversian canal. a(iv) and b(iv) Show the FIB-SEM BSE images with the inset showing the FIB image of the milled region. In a(v) and b(v), the gray value frequency distributions for the corresponding 3D FIB-SEM image stacks are depicted. The inset in a(iv) shows the sketch of a typical cylindrical osteon with a coordinate system valid for all images.

In order to investigate the permanence of the iodine staining, sample #5 (which had been treated according to protocol #5) was stored in an open container in a fume hood under ambient conditions for 18 months. Afterward, another osteon in this sample was imaged (osteon #2). As shown in Figure 3c, the contrast between the osteoid and the PMMA diminished and the peaks of the osteoid and the PMMA are merged in the gray value frequency distribution (see the left peak in Figure 3d).

The effect of the amount of iodine on the tissue staining and image quality was tested by increasing the amount of solid iodine to $50 \text{ mg}^{[31]}$ in one step with 1 week incubation time (protocol #6). **Figure 4** shows ESEM and FIB-SEM BSE images of a forming osteon stained following this protocol. **Figure 4c,d** show that, first, iodine preferentially stained the surface of the sample forming a roughly $3 \mu\text{m}$ thick layer. Second, iodine poorly penetrated the sample leaving most of the osteoid unstained and therefore black in the image. Third, iodine also penetrated within the

PMMA, giving rise to white patches (left in **Figure 4c,d**). It is therefore concluded that, for volume imaging, excessive iodine exposure cannot be used to shorten staining times, particularly because it is not suitable for achieving homogenous staining of the osteoid underneath the sample surface.

2.4. Surface Effects of Iodine Staining

Focusing on iodine-related changes on the sample surface, a heterogeneous staining pattern was observed in ESEM images immediately after the first staining step of protocol #1 (i.e., 0.1 mg of iodine within 6 days of incubation time). **Figure 5a, b** shows the very same sample region before (**Figure 5a**) and just after (**Figure 5b**) this staining step. The brightness changes reveal the lamellar structure of some osteons (the red asterisks in **Figure 5b**) and often brighten the appearance of the boundaries

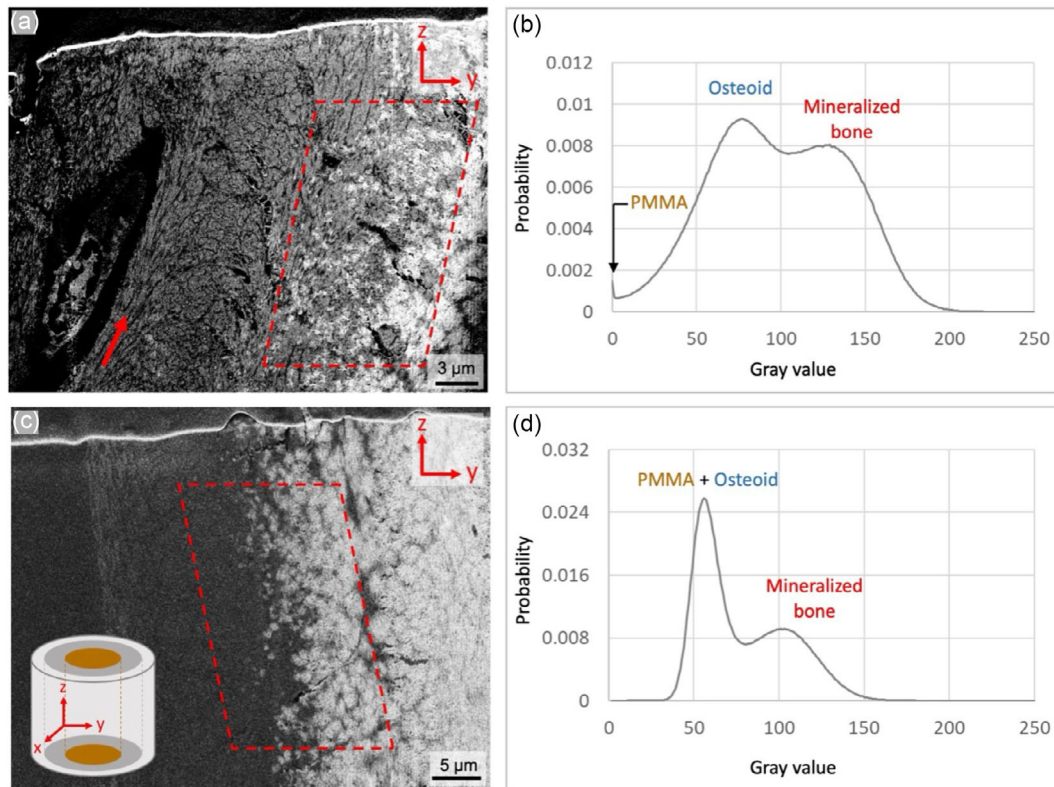


Figure 3. a) FIB-SEM BSE image of a mineralizing bone matrix after staining according to protocol #5 (osteon #1 of sample #5). The mineralized bone (bright) and osteoid (gray) are visible. The preferred orientations of the fibrous collagen matrix can also be distinguished (marked by the red arrow indicating an in-plane orientation). b) The gray value frequency distribution of the 8 μm thick subvolume indicated by the red dashed lines in (a). The volume was chosen in order to contain roughly half osteoid and half mineralized bone which provides corresponding peaks in the gray value frequency distribution. As the gray value of the dark regions in the parallelogram (mainly canaliculi filled with PMMA) is near zero, the PMMA phase piles up at zero. c) FIB-SEM BSE image of a forming osteon (osteon #2 of sample #5), which was measured after leaving the sample for 18 months. The inset shows the sketch of a typical cylindrical osteon with a coordinate system valid for both images in (a,c). d) The gray value frequency distribution of a similar region of interest in comparison with (a) shown by the red dashed lines in (c).

of the osteons (the black asterisks in Figure 5b). Notably, these stained regions are wider than the cement lines, which exhibit a thickness of only 1-5 μm.^[38] Specific regions of interstitial bone and some osteons are intensely stained (green arrows in Figure 5b), but no clear correlation between staining intensity and the degree of mineralization (e.g., BSE brightness before staining) was observed.

As the staining pattern on the surface is clearly influenced by orientational effects such as the lamellar structure of the osteons, second harmonic generation (SHG) imaging was performed, as this technique is commonly used to detect regions of highly ordered,^[39] in-plane oriented,^[40] parallel^[41] collagen fibers. The SHG image shown in Figure 5c clearly exhibits the lamellar structure of the osteons and interstitial bone regions and confirms that often neighboring lamellae exhibit different brightness levels after staining. A spatial correlation between the ESEM and SHG image shows that bright lamellae can be clearly associated with each other in both images, indicating that in-plane ordered collagen fibers are more prone to accumulating iodine at their surface than the regions with collagen fibers with an out-of-plane orientation.

It should be noted that the heterogeneous staining of the sample surface (ESEM information depth $\approx 0.5 \mu\text{m}$, see Experimental Section) is not in contradiction with the nondetectable heterogeneity of the in-depth staining of the osteoid seam. It appears that mineralized regions on the block surface which are in direct contact with the iodine vapor stain differently depending on the collagen orientation. On the other hand, the staining intensity below the sample surfaces of the osteoid seam was found to be homogenous when employing an appropriate protocol (see Figure 1d).

3. Discussion

In this study, possible strategies for staining PMMA-embedded bone samples with iodine vapor were investigated. By varying parameters, such as the amount of iodine, exposure time, and post/pre-CLSM imaging (Table 1), a protocol to enhance Z contrast between the osteoid and the embedding material was developed. Given that the bone sample was stained with rhodamine before embedding, CLSM imaging of the LCN can be performed in addition to 3D BSE imaging. The combination of information

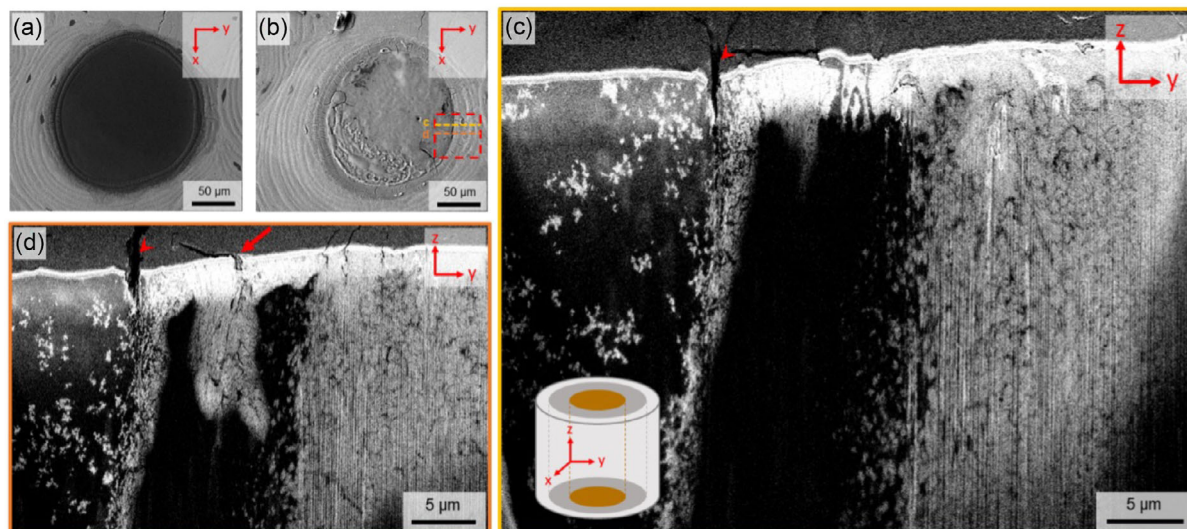


Figure 4. Effect of excessive staining with iodine. ESEM image of a forming osteon of sample #6 a) before and b) after iodine staining, with an exposure of the sample to 50 mg of iodine (protocol #6). The dashed red rectangle shows the region of interest milled by a FIB. The yellow and orange dashed lines within the region of interest represent the position of two different slices of the FIB-SEM image stack shown in c,d). (c) In the BSE image, three different regions can be discriminated in the forming osteon: the Haversian canal filled with PMMA (left region), the osteoid (middle region), and mineralized bone (right region). The osteoid below the surface was not stained with iodine and therefore appears black. In contrast, a surface layer with about 3 μm thickness at the surface was overstained. The red arrow in (d) indicates a microcrack at the surface where iodine could have more easily penetrated. Also, a microcrack at the interface of the PMMA and osteoid is visible where the osteoid is more stained with iodine (see the arrowheads in (c,d)). The inset shows the sketch of a typical cylindrical osteon with a coordinate system valid for all images.

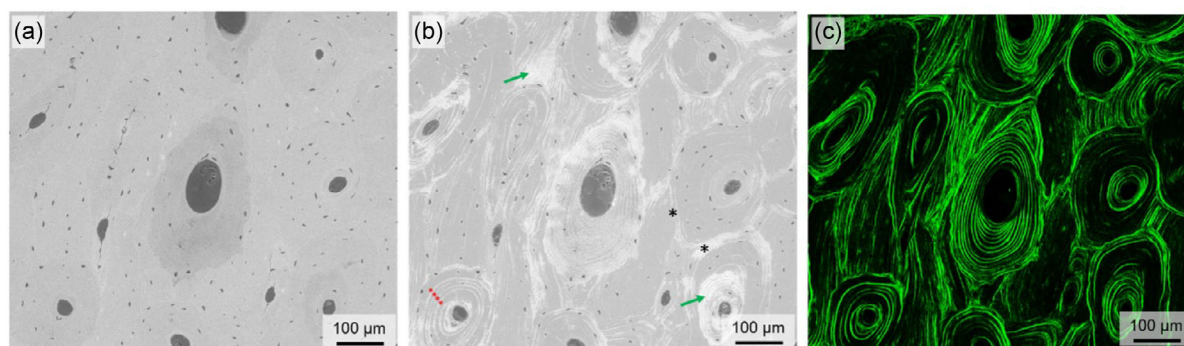


Figure 5. Surface effects of iodine staining on bone tissue. ESEM image of an osteon (osteon #1 of sample #7) in the center a) before and b) immediately after one cycle of iodine staining with an exposure of the sample to 0.1 mg of iodine within 6 days (protocol #1). Interesting bright regions are highlighted by symbols: lamellae in an osteon (red asterisks), the boundaries of osteons (black asterisks), and specific osteons and regions of interstitial bone (green arrows). c) SHG image of the same region showing the lamellar structure of osteons.

gained by the two techniques can be used to study cell–matrix relationships from the micro- to the nanoscale. The information about the LCN architecture is also a prerequisite for predicting the fluid flow through the network and hence the local mechanosensitivity of the bone.^[42] It should be emphasized that this approach can be extended by additional techniques to obtain a more detailed 3D characterization of the (un)mineralized bone. In such a multimodal approach, microcomputed tomography could provide information about the macro- and microporosity of the investigated bone, while tomographic X-ray scattering allows a 3D characterization of the sizes and arrangement of the nanoscopic mineral particles of bone.^[43,44]

By exploring the aforementioned parameters for the staining protocol, an appropriate set of parameters was found, which offers 3D imaging of bone with the following properties: 1) discrimination between the osteoid and the embedding material, PMMA; 2) 3D spatially homogeneous staining for FIB-SEM, which proved a valuable technique for studying the relationship between the matrix, minerals, and LCN;^[15,33,45–49] 3) relatively short staining times (roughly 2 weeks) resulting in optimal Z contrast for simple histogram-based 3D segmentation of the LCN; and 4) repeatable cycles for deeper and more intense staining.

Several scenarios have been reported for binding iodine to osteoid including:^[31] 1) reduction of iodine to iodide and

triiodide ions and formation of ionic bonds with cations, 2) formation of complexes with reactive polysaccharides, i.e., starch and glycogen, 3) replacement of covalently bound halogen atoms, e.g., chlorine, and 4) alkene halogenation, i.e., formation of organoiodine compounds when iodine reacts with carbon-carbon double bonds. In the case of dehydrated osteoid, which is mainly composed of collagen, noncollagenous proteins, and proteoglycans, carbon-carbon double bonds are more likely involved in binding with iodine. Hence, the overstaining of the osteoid in protocol #4 (performing CLSM followed by iodine staining) might be explained by the effect of laser irradiation on the matrix. Additional carbon-carbon double bonds might be formed by the exposure to intense light. Under laser irradiation, in fact, the local temperature of the investigated tissue could raise significantly and this could promote/increase the reactivity of reducing sugars and free amines, which can participate in Maillard-type reactions.^[50] This would result in the generation of melanoidins, which contain carbon-carbon double bonds. It was also found that the staining protocols are partly reversible (Figure 3c), which is probably due to the fact that in the presence of an excess of iodine in the reaction vessel, the iodine oxidizes the carbon-carbon double bond leading to an iodine addition. However, when the staining is completed and the partial pressure of the iodine vapor becomes very small, the iodine is oxidized again to I₂, after which the halogen addition can be slowly reversed and the original alkene bond reformed.

The strength of the presented protocol is that it provides simultaneous 3D analysis of osteoid and mineralized bone with the option for multimodal imaging if CLSM is desired for mapping larger regions of the LCN. This approach facilitates the 3D investigation of physiological biomineralization of bone in humans (see ref. [33]) but is likewise applicable to diverse animal models. As for pathological mineralization, specific targets of interest are bone diseases, which are linked to a dysfunctional mineralization process. A prominent example is osteomalacia, which is characterized by an excessive presence of unmineralized bone. Cases linked to severe osteomalacia are observed in

Phospho1 knockout mice,^[51] klotho and FGF32 deficient mice,^[52] vitamin D deficiency,^[53] and tumor induced phosphate wasting,^[54] among other cases. It has been reported that in X-linked hypophosphatemia, which is the most common heritable form of rickets/osteomalacia, local hypomineralization can occur around the LCN resulting in significantly lower mineral content compared to healthy tissue.^[55] The present approach can address the important question of whether the observed dysfunction in the mineralization process is linked more to a disturbed formation of new mineralization foci, or the growth of such foci (or both). In many cases, it might not be necessary to design new studies, but rather to reinvestigate resin-embedded and archived samples. This possibility is a significant advantage of the presented protocol compared to most other approaches and makes its application very attractive, not only from a scientific point of view but also from an ethical and financial standpoint.

4. Conclusion

Iodine vapor staining is a compelling approach for a homogeneous contrast enhancement of BSE FIB-SEM imaging of embedded mineralized tissues, such as bone, in which visualization of the mineralized/unmineralized interfaces is challenging. Visualization and analysis of the unmineralized tissue are particularly essential for clinically relevant PMMA-embedded specimens. By using the presented staining protocol, not only can such specimens be imaged with FIB-SEM, but also with CLSM in a correlative fashion, allowing for the analysis of the osteocyte LCN and its surrounding extracellular matrix (Figure 6). Nonetheless, to avoid undesired staining effects such as overstaining and inhomogeneous staining, sample preparation and correlative imaging of bone tissue must be performed in the correct order as follows: 1) rhodamine staining, 2) PMMA embedding, 3) iodine staining, 4) CLSM imaging, and 5) FIB-SEM imaging. Moreover, the amount of iodine and exposure time, as the key parameters of iodine vapor staining, must be carefully applied.

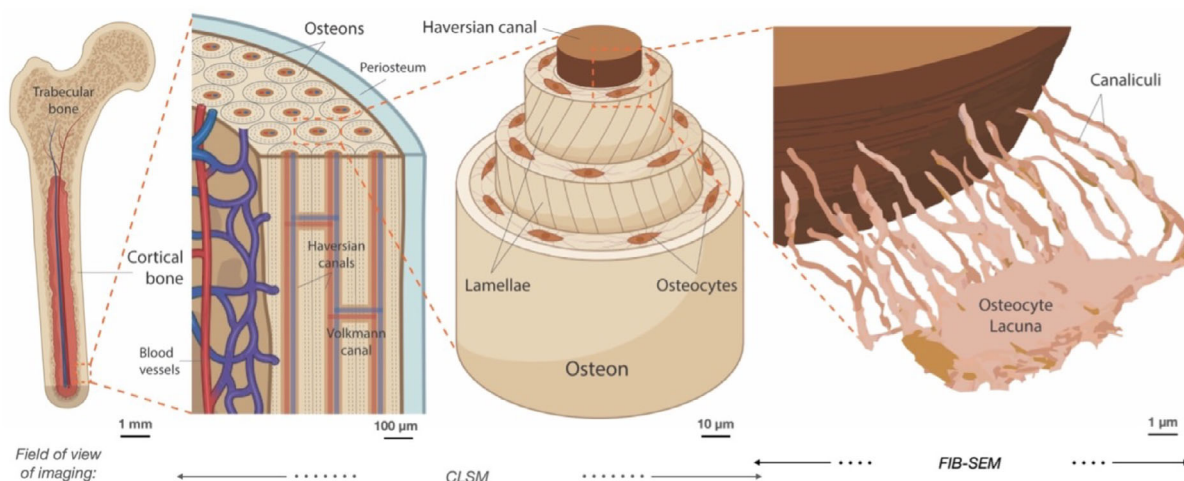


Figure 6. The hierarchical structure of bone. By using CLSM and FIB-SEM in a correlative fashion, the 3D imaging of bone micro/nanostructure and the osteocytes' LCN is possible. While with CLSM one can image the osteons and the LCN within an individual osteon in the cortical bone, with FIB-SEM a single osteocyte lacuna and its canaliculi can be imaged (created with BioRender and Adobe illustrator).

5. Experimental Section

Sample Preparation: Postmortem bone samples from the femoral midshaft of five women were obtained from the Department of Forensic Medicine and the Department of Anatomy at the Medical University of Vienna according to the university's ethic commission regulations (EK no. 1757/2013). The individuals were near the onset of menopause (ages given in years were: sample #1 = 48 y, sample #2 = 55 y, sample #3 = 56 y, samples #4, #5, and #6 (all from one donor) = 51 y, and sample #7 = 50y). A mouse femur sample was used in addition to the human femoral samples (see Supporting Information for the details of sample preparation). Immediately after dissection, the bones were frozen and stored at -20°C . After unfreezing, the samples were cleaned of bone marrow and residual flesh and a 1 cm thick piece of the diaphysis was cut perpendicular to the long axis of the bone. A gradual ethanol dehydration series was performed (80%, 90%, 95%, and 100% at 24 h per step) to minimize the formation of cracks due to bone shrinkage. After dehydration, the samples underwent a series of acetone/ethanol immersions including acetone/ethanol (1:1) for 24 h, 100% acetone for 24 h, again acetone/ethanol (1:1) for 24 h, and finally 100% ethanol for 48 h. If the measurement protocol included a measurement of the LCN using CLSM, the samples were put into tubes (50 mL) with a mixture of ethanol and rhodamine (0.417 g rhodamine 6G (Acros Organics, Geel – Belgium)/100 mL ethanol). The tubes were mounted overnight on a low-speed spinning wheel to provide optimal penetration of the staining fluid. This procedure was repeated 3 times, each with a fresh ethanol–rhodamine mixture, to provide the highest possible stain concentrations in the samples. The stained samples were then embedded in PMMA (Carl Roth GmbH + Co. KG, Karlsruhe, Germany) as described previously.^[56] The embedding protocol includes 1) infiltration of the samples with pure MMA on a shaker at room temperature for 3 days; 2) transferring the samples into a mixture of MMA, benzoyl peroxide, and dibutyl phthalate for 2 days; 3) transfer into an incubation chamber for polymerization while increasing the temperature from 34 to 50°C over 5 days. Due to the low viscosity and water miscibility of PMMA, it easily penetrates through large and small porosities, such as Haversian canals and the LCN. After embedding, a sector was cut out of the sample block by performing two longitudinal cuts, which was then cut perpendicular to the long axis of the bone with a low-speed diamond saw (Buehler Isomet, Lake Bluff, Illinois). Hence, approximately $5 \times 5 \text{ mm}^2$ sized and 1 mm thick slices were obtained, in which roughly circular cross sections of osteons were exposed at the surface. The samples were then ground with sandpaper of different grain sizes and polished with 3 and 1 μm grain sized diamond suspensions using an automatic grinding machine (Logitech PM5, Glasgow, Scotland).

Iodine Staining: Iodine staining was performed postembedding using an iodine vapor phase. Solid iodine (Alfa Aesar, Karlsruhe, Germany) and the sample block were put in a 25 mL glass vessel sealed with PTFE tape. Immediately after incubation, the color of the surrounding atmosphere changed to light pink, which was an indication of iodine sublimation^[57] (see Table 1 for more details on the amount of iodine and the incubation time of different protocols). To ensure a homogenous staining, and to avoid overstaining of the osteoid, the iodine vapor pressure was kept below the saturation point. To determine these conditions, the amount of iodine that theoretically produces a saturated vapor pressure was calculated by assuming that iodine vapor and air inside the container create an ideal gas mixture. This calculation follows from Dalton's law of partial pressures under the assumption of ideal gases.^[58]

$$P_A = X_A P \quad (1)$$

where P_A is the partial pressure of component A in a gas mixture with two components, X_A the mole fraction of A, and P the total pressure. The component A was determined to be gaseous iodine and the component B to be air. Given that P_A , the saturated vapor pressure of iodine at 25°C , is only 40.66 Pa,^[59] i.e., much smaller than the atmospheric pressure P (101 325 Pa), the mole fraction of A, $X_A = \frac{n_A}{n_A + n_B}$, can be expressed as $X_A \cong \frac{n_A}{n_B}$, where n_A denotes the moles of iodine and n_B the moles of air molecules in the gas mixture, and therefore:

$$n_A = n_B \frac{P_A}{P} \quad (2)$$

n_B , the number of moles of air in a 25 cm^3 container can be calculated from the ideal gas law to be around 1.022 mmol. From this calculation, it follows that n_A (which is the moles of iodine at saturation in the vessel) is 4.1×10^{-4} mmol. By multiplying with the molecular weight of iodine (12, 253.8089 g mol^{-1}), the amount of iodine that sublimates to vapor and produces saturated vapor pressure is calculated to be 0.1 mg. It should be noted that this is a theoretical value which does not consider any sinks for the iodine gas molecules nor assumes an immediate sublimation of all of the solid iodine. In the experiment, using 0.1 mg of iodine or less guarantees that the atmosphere is not iodine saturated, because the sublimation of the solid takes some time and at least part of the iodine will accumulate in the sample (protocols #1–#4). For testing protocols #1–#4, the aim was to stay below the saturation point to avoid overstaining. Hence, ≈ 0.1 mg solid iodine was added followed by 6 days of incubation time. As a previous report by Boyde et al.^[31] indicates beneficial effects of longer staining times (20 days to 2 months), the staining cycle was repeated to ensure a high penetration depth below the surface (see Table 1). A time lag of 4–24 days between the staining cycles was implemented for samples #1–#4. In order to test the effect of stronger (i.e., longer durations and higher concentrations) iodine exposure, for protocol #5 staining was performed with 8 mg of iodine during 35 days in four steps with 2 mg added at day 0, day 6, day 9, and day 26, respectively. The samples were checked with ESEM to track the staining at each step including a final check at day 35, before starting the FIB-SEM preparation (Figure 3a). In protocol #6, we tested the effect of excessive amount of iodine on the tissue staining by adding 50 mg of solid iodine to the vessel in one step, which was then left to incubate with the sample for 1 week (Figure 4). Similar to other protocols, ESEM and FIB-SEM were utilized to check stained tissue.

ESEM: The polished surfaces of uncoated samples were imaged with ESEM (FEI Quanta 600, USA) in the BSE mode to select forming osteons. The BSE yield of a typical forming osteon is lower compared to a mature fully mineralized osteon due to lower mineral content of the recently deposited matrix. To check if the osteoid of forming osteons was stained with iodine, i.e., to track changes in brightness, the samples were also imaged after iodine staining and before FIB-SEM. For each sample, after providing an overview image with $50\times$ magnification (2.6 μm pixel size), the selected forming osteons were imaged with $600\times$ magnification (270 nm pixel size). The measurements were performed under low pressure (1 mbar) with 12.5 kV acceleration voltage and ≈ 10 mm working distance.

According to Monte Carlo simulations and calculations presented by Goldstein et al. (Kanaya–Okayama radius),^[60] we can estimate that the main origin of BSEs in the presented measurements is restricted to a 0.5 μm thick layer below the surface.

CLSM: On forming osteons selected by ESEM imaging, CLSM was used to image the LCN in rhodamine-stained bone tissue.^[61] The measurement was conducted with an inverted TCS SP8 (Leica, Wetzlar, Germany) equipped with an oil immersion lens (HC PL APO $40\times/1.30$ OIL) following an earlier developed protocol.^[36,37,62] For the excitation of rhodamine, the 514 nm line of an argon laser was used, and the fluorescence signal was measured in a spectral window between 540 and 620 nm with an airy 1 pinhole of 65.4 μm . 3D image stacks were obtained with an isotropic voxel size of 0.31 μm , where each image size was $317 \times 317 \mu\text{m}^2$ and imaging depth 40–50 μm . The scan speed was 200 lines per second. To achieve a constant brightness and contrast within each dataset and to compensate for the loss of signal observed while imaging through the depth of the sample, the laser intensity and the photomultiplier gain were correspondingly increased.

SHG Imaging: Collagen fibrils in bone exhibit SHG signals due to their noncenter symmetric molecular structure, the anisotropic macromolecular organization^[63] and the specific orientation of the light polarization with respect to the collagen fibrils.^[64,65] To determine the positions of the lamellae within multiple osteons, second harmonic imaging was performed using a SP8 confocal microscope (Leica Microsystems, Wetzlar,

Germany) with a 40× oil immersion lens (HC PL APO CS2 40×/1.3 oil, Leica Microsystems, Wetzlar, Germany). The SHG signal was generated using a Mai-Tai high performance Ti:Sa Laser (Spectra-Physics, Milpitas, CA, USA) operating at a wavelength of 910 nm. The signal was detected at 450–460 nm (half the excitation wavelength).

FIB-SEM: To validate the homogeneity of iodine staining in depth of the samples and to obtain 3D image stacks, FIB-SEM (Crossbeam 540 Zeiss, Oberkochen, Germany) was used. The samples were first carbon coated (thickness of ≈15 nm) by a vacuum carbon evaporator sputter coater (Bal-tec/Balzers, Liechtenstein, Germany). Afterward, to ensure that the samples did not undergo shrinkage due to dehydration during the measurement performed under high vacuum (10^{-6} mbar) conditions, the samples were mounted inside the vacuum chamber at least 24 h before image acquisition. The working distance was set to 5.1 mm (which is the distance between the coincidence point of ion and electron beams, and the lower polepiece surface of the electron microscope). The milling process was conducted with high- and low-current gallium ion probes, i.e., 30–65 and 0.7–3.0 nA, at 30 kV acceleration voltage, respectively. With the former, a trench ($\approx 100 \times 100 \times 100 \mu\text{m}^3$) was rapidly milled (≈ 10 min), while with the latter, the final region of interest ($\approx 40 \times 30 \times 50 \mu\text{m}^3$) was finely sliced to acquire the 3D image stack. The milling depth was at least 50 μm for mineralized bone tissue in all samples. In the serial surface imaging mode, images with spatial resolution of $\approx 40 \times 40 \times 40 \text{ nm}^3$ were obtained with 2–2.5 kV electron acceleration voltage and 500–1000 pA electron beam current. The acquisition time per image was 28 s, and the images were acquired using 40 averaging cycles per line. 8-bits secondary and BSE images were simultaneously recorded, and the brightness and contrast were set such that no regions were over- or underexposed. In total, seven samples, including six human (samples #1–#6) and one mouse bone, were measured, from which 16 image stacks were acquired (see Table 1). 3D image stacks of samples #1, #2, and #3 were used in our previous study on forming osteons.^[33]

Image Processing: Image processing of the FIB-SEM BSE images was performed to clean the image from artifacts resulting from 1) misalignment/sample drift, 2) image noise, and 3) inhomogeneous milling resulting in curtaining artifacts.^[66–69] In-house developed Python scripts (Version 3.7, Python Software Foundation, Delaware, United States) were applied in three steps: 1) Alignment: To align the images with respect to each other to correct sample drifts, we used ORB (Oriented FAST and Rotated BRIEF)^[70] as a key point extractor and FLANN (Fast Library for Approximate Nearest Neighbors) as a matcher as implemented in OpenCV (v. 3.4). Key points (such as corners) were detected by FAST (features from accelerated segment test) using variations in the intensity of pixels. After detection of the key points, BRIEF (Binary Robust Independent Elementary Features) was used as a key point descriptor which provided the locations of the same key points in another image. FLANN was then used to match the described key points.^[71] 2) Denoising: To enhance the signal-to-noise ratio of the images, denoising was performed using a total variation method (Chambolle algorithm^[72]) as implemented in the scikit-image package v. 0.16. 3) Destriping: To eliminate curtaining artifacts, we implemented an algorithm based on pyWavelets v. 1.0.1 for the wavelets decomposition and based on numpy 1.16 for the calculation of the Fourier transforms.^[73]

Supporting Information

Supporting Information is available from the Wiley Online Library or from the author.

Acknowledgements

This study was supported by the AUVA (research funds of the Austrian workers' compensation board) and OEGK (Austrian health insurance fund). P.F. and R.W. acknowledge support from the Max Planck Queensland Centre for the Materials Science of Extracellular Matrices. The authors are grateful to Dr. Amaia Cipitria for providing the mouse

sample. The authors also thank Heike Runge, Birgit Schonert, Gabriele Wienskol, Daniela Gabriel, Sonja Lueger, Petra Keplinger, and Phaedra Messmer for careful sample preparation. Part of the volume imaging data was acquired at the CoreLab Correlative Microscopy and Spectroscopy at Helmholtz-Zentrum Berlin (HZB) für Materialien und Energie. The authors are grateful for the help and cooperation of Dr. Katja Höflich and Holger Kropf at HZB in the data acquisition. The authors are highly indebted to Prof. Alan Boyde, Queen Mary University London, for discussions about iodine staining. The authors would like to extend their gratitude to Lisa D. Camp and Stephan Sutter from Cornell University for their assistance with the final proofreading of the manuscript.

Conflict of Interest

The authors declare no conflict of interest.

Data Availability Statement

The data that support the findings of this study are openly available in [EDMOND] at [https://doi.org/10.17617/3.DTCRQT], reference number [0].

Keywords

3D imaging, contrast enhancement, focused ion beam-scanning electron microscopy, iodine vapor staining, lacunocanalicular network, osteocytes, osteoid

Received: February 27, 2024

Revised: June 19, 2024

Published online: July 17, 2024

- [1] S. Weiner, E. Raguin, R. Shahar, *Nat. Rev. Endocrinol.* **2021**, *17*, 307.
- [2] P. Fratzl, *Nature* **2015**, *527*, 308.
- [3] M. Dierolf, A. Menzel, P. Thibault, P. Schneider, C. M. Kewish, R. Wepf, O. Bunk, F. Pfeiffer, *Nature* **2010**, *467*, 436.
- [4] P. Goggin, E. M. L. Ho, H. Gnaegi, S. Searle, R. O. C. Oreffo, P. Schneider, *Bone* **2020**, *131*, 115107.
- [5] P. Schneider, M. Meier, R. Wepf, R. Müller, *Bone* **2011**, *49*, 304.
- [6] M. A. Hayat, *Principles and Techniques of Electron Microscopy: Biological Applications*, Edward Arnold, London **1981**.
- [7] A. Boyde, *Bone Research Protocols*, Springer, New York **2019**, pp. 571–616.
- [8] J. D. Currey, *Bones: Structure and Mechanics*, Princeton University Press, Princeton **2006**.
- [9] M. Maglio, F. Salamanna, S. Brogini, V. Borsari, S. Pagani, N. Nicoli Aldini, G. Giavaresi, M. Fini, *Biomed Res. Int.* **2020**, *2020*, 1804630.
- [10] T. Goldschlager, A. Abdelkader, J. Kerr, I. Boundy, G. Jenkin, *J. Visualized Exp.* **2010**, *35*, e1707.
- [11] D. C. Pease, *Histological Techniques for Electron Microscopy*, Academic Press **2013**.
- [12] P. M. Goggin, K. C. Zygalkakis, R. O. C. Oreffo, P. Schneider, *Eur. Cells Mater.* **2016**, *31*, 264.
- [13] D. Chappard, S. Palle, C. Alexandre, L. Vico, G. Riffat, *Acta Histochem.* **1987**, *81*, 183.
- [14] O. Zhanmu, X. Yang, H. Gong, X. Li, *Sci. Rep.* **2020**, *10*, 12639.
- [15] A. R. Spurr, *J. Ultrastruct. Res.* **1969**, *26*, 31.
- [16] J. H. Luft, *J. Biophys. Biochem. Cytol.* **1961**, *9*, 409.
- [17] P. Vickerton, J. Jarvis, N. Jeffery, *J. Anat.* **2013**, *223*, 185.
- [18] K. Degenhardt, A. C. Wright, D. Horng, A. Padmanabhan, J. A. Epstein, *Circ.: Cardiovasc. Imaging* **2010**, *3*, 314.

- [19] A. Boyde, E. Maconnachie, S. A. Reid, G. Delling, G. R. Mundy, *Scanning Electron Microsc.* **1986**, 1986, 31.
- [20] H. E. Gruber, G. J. Marshall, M. E. Kirchen, J. Kang, S. G. Massry, *Stain Technol.* **1985**, 60, 337.
- [21] P. G. T. Howell, K. M. W. Davy, A. Boyde, *Scanning* **1998**, 20, 35.
- [22] P. Roschger, H. Plenck Jr, K. Klaushofer, J. Eschberger, *Scanning Microsc.* **1995**, 9, 4.
- [23] J. G. Stempak, R. T. Ward, *J. Cell Biol.* **1964**, 22, 697.
- [24] W. Ribi, T. J. Senden, A. Sakellariou, A. Limaye, S. Zhang, *J. Neurosci. Methods* **2008**, 171, 93.
- [25] B. D. Metscher, *BMC Physiol.* **2009**, 9, 11.
- [26] E. Beniash, W. Traub, A. Veis, S. Weiner, *J. Struct. Biol.* **2000**, 132, 212.
- [27] Z. Zou, W. Rong, S. Wei, Y. Ji, L. Duan, *Proc. Natl. Acad. Sci.* **2020**, 117, 29462.
- [28] M. Nierenberger, Y. Rémond, S. Ahzi, P. Choquet, *C. R. Biol.* **2015**, 338, 425.
- [29] N. S. Jeffery, R. S. Stephenson, J. A. Gallagher, J. C. Jarvis, P. G. Cox, *J. Biomech.* **2011**, 44, 189.
- [30] H. Haimov, E. Shimoni, V. Brumfeld, M. Shemesh, N. Varsano, L. Addadi, S. Weiner, *Bone* **2020**, 130, 115086.
- [31] A. Boyde, F. A. Mccorkell, G. K. Taylor, R. J. Bompfrey, M. Doube, *Microsc. Res. Tech.* **2014**, 77, 1044.
- [32] A. Boyde, *Eur. Cells Mater.* discussion 160-1 **2012**, 24, 154.
- [33] M. Ayoubi, A. F. Van Tol, R. Weinkamer, P. Roschger, P. C. Brugger, A. Berzlanovich, L. Bertinetti, A. Roschger, P. Fratzl, *Adv. Healthcare Mater.* **2021**, 10, 2100113.
- [34] V. A. J. Jaques, A. D. Plessis, M. Zemek, J. Šalplachta, Z. Stubianová, T. Zikmund, J. Kaiser, *Meas. Sci. Technol.* **2021**, 32, 122001.
- [35] F. Repp, P. Kollmannsberger, A. Roschger, A. Berzlanovich, G. M. Gruber, P. Roschger, W. Wagermaier, R. Weinkamer, *J. Struct. Biol.* **2017**, 199, 177.
- [36] A. F. van Tol, A. Roschger, F. Repp, J. Chen, P. Roschger, A. Berzlanovich, G. M. Gruber, P. Fratzl, R. Weinkamer, *Biomech. Model. Mechanobiol.* **2019**, 19, 823.
- [37] A. Roschger, P. Roschger, W. Wagermaier, J. Chen, A. F. Van Tol, F. Repp, S. Blouin, A. Berzlanovich, G. M. Gruber, K. Klaushofer, P. Fratzl, R. Weinkamer, *Bone* **2019**, 123, 76.
- [38] D. B. Burr, M. B. Schaffler, R. G. Frederickson, *J. Biomech.* **1988**, 21, 939.
- [39] A. Erikson, J. Örtengren, T. Hompland, C. De Lange Davies, M. Lindgren, *J. Biomed. Opt.* **2007**, 12, 044002.
- [40] R. Genthial, E. Beaufort, M.-C. Schanne-Klein, F. Peyrin, D. Farlay, C. Olivier, Y. Bala, G. Boivin, J.-C. Vial, D. Débarre, A. Gourrier, *Sci. Rep.* **2017**, 7, 3419.
- [41] P. Stoller, P. M. Celliers, K. M. Reiser, A. M. Rubenchik, *Appl. Opt.* **2003**, 42, 5209.
- [42] A. F. Van Tol, V. Schemenz, W. Wagermaier, A. Roschger, H. Razi, I. Vitienes, P. Fratzl, B. M. Willie, R. Weinkamer, *Proc. Natl. Acad. Sci. U. S. A.* **2020**, 117, 32251.
- [43] M. Liebi, M. Georgiadis, A. Menzel, P. Schneider, J. Kohlbrecher, O. Bunk, M. Guizar-Sicairos, *Nature* **2015**, 527, 349.
- [44] P. De Falco, R. Weinkamer, W. Wagermaier, C. Li, T. Snow, N. J. Terrill, H. S. Gupta, P. Goyal, M. Stoll, P. Benner, P. Fratzl, *J. Appl. Crystallogr.* **2021**, 54, 486.
- [45] N. Reznikov, R. Almany-Magal, R. Shahar, S. Weiner, *Bone* **2013**, 52, 676.
- [46] Y. Haridy, M. Osenberg, A. Hilger, I. Manke, D. Davesne, F. Witzmann, *Sci. Adv.* **2021**, 7, eabb9113.
- [47] D. M. Binkley, J. Deering, H. Yuan, A. Gourrier, K. Grandfield, *J. Struct. Biol.* **2020**, 212, 107615.
- [48] N. Reznikov, R. Shahar, S. Weiner, *Bone* **2014**, 59, 93.
- [49] D. J. Buss, N. Reznikov, M. D. Mckee, *J. Struct. Biol.* **2020**, 212, 107603.
- [50] T. Dutton, M. Orcutt, *J. Chem. Educ.* **1984**, 61, 303.
- [51] A. Boyde, K. A. Staines, B. Javaheri, J. L. Millan, A. A. Pitsillides, C. Farquharson, *J. Anat.* **2017**, 231, 298.
- [52] S. K. Murali, P. Roschger, U. Zeitz, K. Klaushofer, O. Andrukhova, R. G. Erben, *J. Bone Miner. Res.* **2016**, 31, 129.
- [53] A. Bhan, A. D. Rao, D. S. Rao, *Rheum. Dis. Clin. North Am.* **2012**, 38, 81.
- [54] K. Nawrot-Wawrzyniak, F. Varga, A. Nader, P. Roschger, S. Sieghart, E. Zwettler, K. M. Roetzer, S. Lang, R. Weinkamer, K. Klaushofer, N. Fratzl-Zelman, *Calif. Tissue Int.* **2009**, 84, 313.
- [55] T. Boukpepsi, B. Hoac, B. R. Coyac, T. Leger, C. Garcia, P. Wicart, M. P. Whyte, F. H. Glorieux, A. Linglart, C. Chaussain, M. D. Mckee, *Bone* **2017**, 95, 151.
- [56] P. Roschger, P. Fratzl, J. Eschberger, K. Klaushofer, *Bone* **1998**, 23, 319.
- [57] M. Ayoubi, *Ph.D. Thesis*, Technische Universität Berlin **2020**.
- [58] D. R. Gaskell, D. E. Laughlin, *Introduction to the Thermodynamics of Materials*, CRC Press, Boca Raton **2017**.
- [59] G. P. Baxter, C. H. Hickey, W. C. Holmes, *J. Am. Chem. Soc.* **1907**, 29, 127.
- [60] J. I. Goldstein, D. E. Newbury, J. R. Michael, N. W. M. Ritchie, J. H. J. Scott, D. C. Joy, *Scanning Electron Microscopy and X-ray Microanalysis*, Springer, New York **2017**.
- [61] S. L. Dallas, D. S. Moore, *Bone* **2020**, 138, 115463.
- [62] F. Repp, P. Kollmannsberger, A. Roschger, M. Kerschitzki, A. Berzlanovich, G. M. Gruber, P. Roschger, W. Wagermaier, R. Weinkamer, *Bone Rep.* **2017**, 6, 101.
- [63] S. Bancelin, C. Aimé, I. Gusachenko, L. Kowalczyk, G. Latour, T. Coradin, M.-C. Schanne-Klein, *Nat. Commun.* **2014**, 5, 4920.
- [64] S. Roth, I. Freund, *J. Chem. Phys.* **1979**, 70, 1637.
- [65] R. M. Williams, W. R. Zipfel, W. W. Webb, *Biophys. J.* **2005**, 88, 1377.
- [66] H. J. T. Stephensen, S. Darkner, J. Sporning, *Commun. Biol.* **2020**, 3, 81.
- [67] J. Fehrenbach, P. Weiss, C. Lorenzo, *IEEE Trans. Image Process.* **2012**, 21, 4420.
- [68] J. Roels, J. Aelterman, J. De Vylder, H. Luong, Y. Saeys, S. Lippens, W. Philips, in *Int. Symp. Visual Computing*, Springer International **2014**.
- [69] T. H. Loeber, B. Laegel, S. Wolff, S. Schuff, F. Balle, T. Beck, D. Eifler, J. H. Fitschen, G. Steidl, *J. Vac. Sci. Technol., B: Nanotechnol. Microelectron.: Mater., Process., Meas., Phenom.* **2017**, 35, 06GK01.
- [70] Y. Lu, K. Gao, T. Zhang, T. Xu, D. Tang, *PLoS One* **2018**, 13, 0190383.
- [71] M. Muja, D. Lowe, *Flann-Fast Library for Approximate Nearest Neighbors User Manual*, Computer Science Department, University of British Columbia, Vancouver, BC, Canada **2009**, p. 5.
- [72] A. Chambolle, *J. Math. Imaging Vision* **2004**, 20, 89.
- [73] D. Spohner, A. M. Steyer, L. Bertinetti, I. Orlov, L. Benoit, K. Pernet-Gallay, A. Schertel, P. Schultz, *J. Struct. Biol.* **2020**, 211, 107528.
- [74] D. B. Burr, O. Akkus, *Basic and Applied Bone Biology*, Academic Press, London **2014**, pp. 3–25.